Spatial dynamics of helium metastables in sheath or bulk dominated rf micro-plasma jets

B Niermann[1], T Hemke[2], N Y Babaeva[3], M Böke[1], M J Kushner[3], T Mussenbrock[2] and J Winter[1]

[1] Ruhr-Universität Bochum, Institute for Experimental Physics II, Universitätsstraße 150, 44801 Bochum, Germany
[2] Ruhr-Universität Bochum, Institute for Theoretical Electrical Engineering, Universitätsstraße 150, 44801 Bochum, Germany
[3] University of Michigan, Electrical Engineering and Computer Science Department, 1301 Beal Ave, Ann Arbor, MI 48109-2122, USA

E-mail: benedikt.niermann@rub.de

Abstract

Space resolved concentrations of helium He (^{3}S$_1$) metastable atoms in an atmospheric pressure radio-frequency micro-plasma jet were measured using tunable diode laser absorption spectroscopy. The spatial profile of metastable atoms in the volume between the electrodes was deduced for various electrode gap distances. Density profiles reveal the sheath structure and reflect the plasma excitation distribution, as well as the dominance of the α-mode discharge. Gap width variations show the transition from a normal glow plasma to a pure sheath discharge. In order to analyse and verify the experimentally observed profiles of the metastable atoms, a two-dimensional simulation model was set up. Applying an appropriate He/N$_2$/O$_2$ chemistry model, the correlation between the metastable profiles and the underlying excitation mechanisms was obtained.

(Some figures may appear in colour only in the online journal)

1. Introduction

Understanding the energy transfer processes in micro-plasmas is one of the key issues to develop new applications and reliable process control. In this context metastable species play a decisive role. Due to their long lifetime metastables collide more frequently with other particles. The metastable density in micro-discharges is several orders of magnitude lower than the density of the ground-state atoms. However, compared with most other species the density is significant and the electron collision excitation cross sections of some helium levels out of the metastable states exhibit values which are several orders of magnitude larger and have much lower thresholds than those for the ground state [1, 2]. Among these metastable atoms the He (^{3}S$_1$) level plays a decisive role, since helium is used as a feed gas in many micro-discharges. This work reports the measurement and simulation of He (^{3}S$_1$) atoms in

an atmospheric pressure micro-plasma jet, providing a simple design by featuring an α-mode RF discharge between two bare metallic electrodes.

Reliable techniques are needed for the systematic investigation of plasma characteristics and dynamics. This is essential for the optimization of plasma sources and process control. Application of conventional diagnostics, especially invasive ones, is often impossible regarding the small dimensions, high operating pressures and high power densities. In this context absorption spectroscopy is a widely used technique to measure e.g. absolute concentrations of particles in plasma discharges, since it is non-invasive, highly sensitive and provides a sufficient spatial resolution [3, 4]. We have applied tunable diode laser absorption spectroscopy (TDLAS) to record the spectral profiles of the lowest helium metastable state, deducing absolute densities for various discharge conditions [5]. The jet configuration used here is
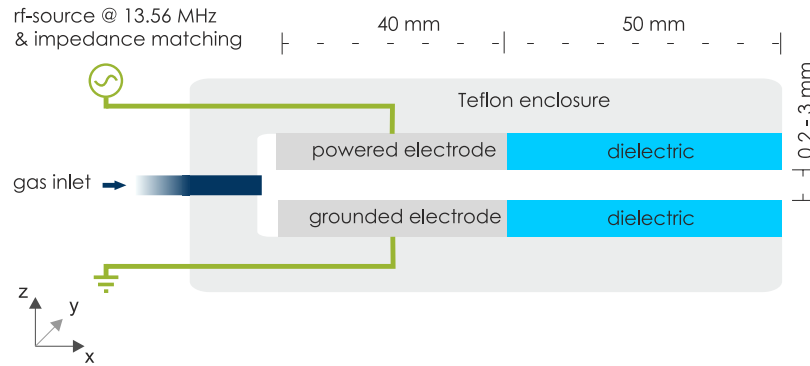
Figure 1. Sketch of the micro-plasma jet discharge, which is also the simulation domain. Shown is a two-dimensional cross-section through plane that is spanned by the two electrodes.

a well analysed and value proven discharge. It was studied already under several experimental and theoretical approaches, describing the discharge characteristics in detail [6–8]. The new approach of the measurements at hand focuses on the variation of the gap width and determination of the sheath/bulk structure and influences on the distribution of excited species in the discharge.

To verify the experimental results and to adequately describe the actual excitation mechanisms a reliable model is needed. By means of the 2D fluid dynamic code *nonPDPSIM* [9] we perform simulations which take into account both the discharge dynamics between the electrodes as well as the influence of the lateral gas flow.

2. The atmospheric pressure micro-plasma jet

The atmospheric pressure micro-plasma jet is a capacitively coupled, non-thermal glow-discharge plasma at high pressures. The design concept of this discharge is based on the plasma jet introduced by Selwyn *et al* in 1998 [10] and advanced by Schulz-von der Gathen *et al* [6] termed μAPPJ. The feed gas flows between two closely spaced stainless steel electrodes driven at 13.56 MHz radio-frequency in a parallel plate configuration (figure 1). Electrodes, plasma volume and effluent are enclosed by quartz windows, giving direct optical access to the plasma itself and the effluent volume behind the electrodes. The discharge uses helium as feed gas with typical gas velocities around 100 m s^{-1}. The electric field between the electrodes causes a breakdown in the gas and produces a plasma with electron temperature and density of about 1–2 eV and 10^{10} cm^{-3}, respectively [7, 8]. Atoms and molecules in the feed gas become excited, dissociated or ionized by electron impacts. Since the electrons are not in thermal equilibrium with the ions and neutrals, the gas temperature remains a few tens Kelvin above room temperature [11].

The presented jet configuration features a dielectric extension of the gas channel to assure controlled gas flow in the effluent behind the plasma. Electrodes and dielectric extensions are 40 mm and 50 mm in length, respectively. The distance between the two windows is fixed to 1 mm while the electrode gap width is variable between 0.2 and 30 mm.

Three distinct modes have to be distinguished in the operation of the discharge: α-, γ- and arc-mode. In the α-mode

the discharge is sustained by bulk ionization, and in front of the electrodes an electron depleted sheath forms [12]. Kong *et al* describe the α-mode structure as consisting of a gap-independent sheath region and a gap-dependent plasma bulk, as long as the gap width is large enough that the sheaths can fully form [13]. At higher RF-powers a breakdown of the sheaths takes place and a so-called γ-mode occurs. The γ-mode is sustained by secondary electron emission especially by Penning ionization, and the sheaths thickness is an order of magnitude smaller [7, 14, 15]. The emission profile exhibits two strong maxima very close to the electrode surfaces. These maxima are usually attributed to the negative glow [12].

Since the parameter space for a stable γ-mode discharge is very narrow, the discharge easily turns into an arc-plasma, characterized by a very constricted plasma between the tips of the electrodes and very high current densities. Our measurements in the parallel plate geometry discharge are restricted to the α-mode operation, since it allows stable long term operation without damaging the system.

2.1. TDLAS set-up

The small dimensions of micro-discharges and their operation at atmospheric pressures are a challenge for optical diagnostics, since high sensitivity and high spatial resolution are required. For the absorption spectroscopic measurements a standard TDLAS set-up was used. The absorption profile was recorded by scanning the laser frequency across the absorption line. Figure 2 shows a sketch of the experimental set-up. The laser beam from the DL passed through two beam splitters. A part of the beam was guided to a Fabry–Perot interferometer (1 GHz free spectral range), a second part through a low pressure reference cell to perform the calibration of the laser frequency. The part of the beam transmitted through the first beam splitter was attenuated by neutral density filters with an optical density in the order of 3, and focused into the discharge with a beam power of less than 2 μW at 100 μm spot size, to avoid any saturation effects. After passing the discharge the beam was guided through a set of apertures and filters to suppress the emission from the plasma by reducing the collection angle and blocking wavelengths different from the observed transitions. The transmitted beam intensity was measured by photodiodes with on-chip transimpedance amplifier. For an effective measurement of the absorption
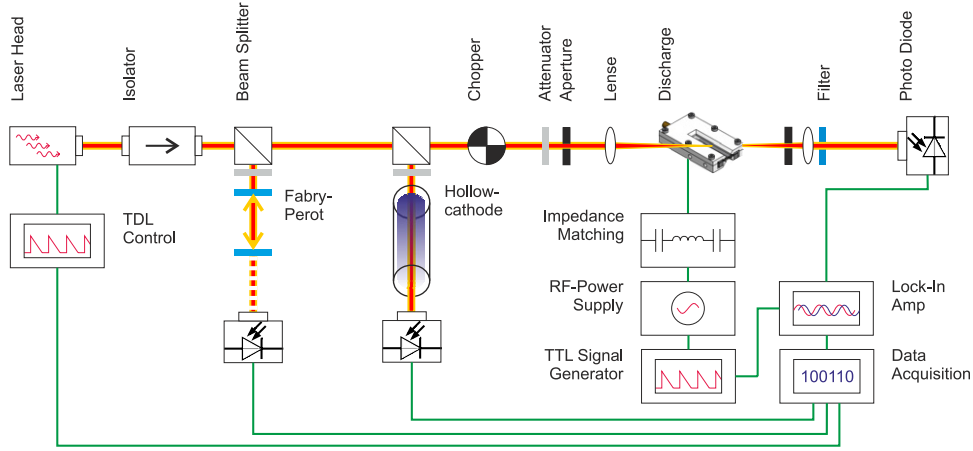
Figure 2. TDLAS set-up.

signal across the jet axes, the discharge casing was mounted on a small movable stage featuring three electronically controlled stepping motors to adjust, with high precision, the discharge cell position in all spatial dimensions. This set-up allows the positioning of the jet with an accuracy of about $5\,\mu m$ and automated xz-mapping of the complete plasma volume (in the y direction all measurements presented in this paper are space averaged).

Since the absorption rate of the laser light by metastable atoms is very low, in the order of 10^{-3} after 1 mm absorption length, lock-in technique was used to measure the changes in signal intensity. Applying lock-in technique requires the pulsing of the signal to be measured. This was realized by pulsing the RF-power coupled into the system, which consequently leads to a pulsing of the metastable density in the discharge. The pulse frequency was chosen to 4 kHz and a duty cycle of 50 %.

Absolute metastable densities were derived from the transmittance I/I_0 and the Beer–Lambert law. Therefore, the four signals

$$L(\nu)\text{—Plasma and Laser on},$$

$$L_0(\nu)\text{—Plasma off, Laser on},$$

$$P(\nu)\text{—Plasma on, Laser off},$$

$$B(\nu)\text{—Plasma and Laser off (background)},$$

have to be acquired to calculate the transmittance spectra and correlate them with the plasma properties by

$$\frac{I(\nu)}{I_0(\nu)} = \frac{L(\nu) - P(\nu)}{L_0(\nu) - B(\nu)} = e^{-k(\nu)l}. \qquad (1)$$

$I(\nu)$ and $I_0(\nu)$ are the intensities of transmitted radiation with and without the presence of absorbing species, $k(\nu)$ is the absorption coefficient and l the path length through the absorbing medium [16]. The absorption coefficient is connected to the population density of metastable atoms by

$$k(\nu) = \frac{1}{4\pi\varepsilon_0} \frac{\pi e^2}{c\,m_e} f_{ik} N_i F(\nu), \qquad (2)$$

where f_{ik} is the oscillator strength of the line, N_i the density of the lower level, and $F(\nu)$ a normalized function

$(\int_0^\infty F(\nu)\,d\nu = 1)$ representing the absorption lineshape. All other terms have their usual definitions. The absolute metastable density can then be given by

$$\int_0^\infty \ln\left(\frac{I_0(\nu)}{I(\nu)}\right) d\nu = S = \frac{e^2 f_{ik}l}{4\epsilon_0 m_e c} N_i, \qquad (3)$$

where S is the area under the absorption curve that provides the line-averaged density of the absorbing species.

2.2. Simulation set-up

The 2D simulations are performed on a non-structured numerical grid with the fluid dynamic code *nonPDPSIM* which has been originally designed and realized by Kushner and co-workers. A detailed description of the code and a number of successful applications can be found in [9, 17–19]. Basic simulations of a radio-frequency driven He/O_2 plasma jet and its effluent accounting for the plasma dynamics and the lateral gas flow can be found in [20]. Here, we just briefly discuss the implemented equations and the underlying physics.

The code *nonPDPSIM* simulates the dynamics of weakly ionized plasmas in the regime of medium to high pressure. It takes into account the physics and chemistry of charged particles—electrons with mass m_e and charge $-e$, ions with mass m_j and charge q_j—and of the excited as well as the ground-state neutrals (mass m_j). For all species j, the continuity equations (particle balances) are simultaneously solved, where $\vec{\Gamma}_j$ is the particle flux density and S_j is the source and loss term, respectively:

$$\frac{\partial n_j}{\partial t} = -\nabla\cdot\vec{\Gamma}_j + S_j. \qquad (4)$$

The fluxes are calculated from the momentum balances in the drift–diffusion approximation evaluated in the local centre-of-mass system. D_j and μ_j are the diffusion constant and the mobility (if applicable) of species j. Further, $\vec{E}$ is the electrical field and $\vec{v}$ is the mass-averaged advective velocity of the medium:

$$\vec{\Gamma}_j = n_j\vec{v} - D_j\nabla n_j + \frac{q_j}{|q_j|}\mu_j n_j \vec{E}. \qquad (5)$$

J. Phys. D: Appl. Phys. **44** (2011) 485204

B Niermann *et al*

For the electron fluid, additionally an energy balance equation is solved taking into account ohmic heating and the energy losses due to elastic and inelastic interaction with the neutrals and ions as well as heat conduction,

$$\frac{\partial}{\partial t}\left(\frac{3}{2}n_{\mathrm{e}}T_{\mathrm{e}}\right) = \vec{j}\cdot\vec{E} - \nabla\cdot\left(-\kappa_{\mathrm{e}}\nabla T_{\mathrm{e}} + \frac{5}{2}T_{\mathrm{e}}\vec{\Gamma}_{\mathrm{e}}\right)$$
$$-n_{\mathrm{e}}\sum_{i}\Delta\epsilon_{i}k_{i}n_{i}. \tag{6}$$

To capture the non-Maxwellian behaviour of the electrons, all electronic transport coefficients (the mobility μ_{e}, the diffusion constant D_{e} and the thermal conductivity κ_{e}) as well as the electronic rate coefficients in equations (4) and (5) are calculated by the local mean energy method: A zero-dimensional Boltzmann equation for the electron energy distribution $f(\epsilon)$ and the transport and rate coefficients is solved for the locally applicable gas composition and various values of the electrical field. The tabulated data are then consulted in dependence of the fluid dynamically calculated electron temperature T_{e}.

The plasma equations are coupled to a modified version of the compressible Navier–Stokes equations which are solved for the gas density ρ, the mean velocity $\vec{v}$, and the gas temperature T. The contributions to the energy equation from Joule heating include only ion contributions; the heat transfer from the electrons is included as a collisional change in the enthalpy. The scalar pressure p is given by the ideal gas law.

Finally, the potential Φ is calculated from Poisson's equation. (The code works in the electrostatic approximation such that $\vec{E} = -\nabla\Phi$.) The charge density on its right hand side stems from the charged particles in the plasma domain and from the bound charges ρ_s at the surfaces. The coefficient $\varepsilon = \varepsilon_0\varepsilon_{\mathrm{r}}$ represents the permittivity of the medium:

$$-\nabla\cdot\varepsilon\nabla\Phi = \sum_{j}q_{j}n_{j} + \rho_{\mathrm{s}}. \tag{7}$$

The surface charges are governed by a separate balance equation, where σ is the conductivity of the solid materials and the subscript s indicates evaluation on the surface:

$$\frac{\partial\rho_{\mathrm{s}}}{\partial t} = \left[\sum_{j}q_{j}(-\nabla\cdot\vec{\Gamma}_{j} + S_{j}) - \nabla\cdot(\sigma(-\nabla\Phi))\right]_{\mathrm{s}}. \tag{8}$$

The dynamical equations are complemented by an appropriate set of boundary conditions. Electrically, the walls are either powered or grounded. With respect to the particle flow, they are either solid, or represent inlets or outlets: The flow is specified to a given flux, while the outlet flow is adjusted to maintain the pressure. Finally, it is worth mentioning that the actual implementation of the equations poses some difficulties due to the vast differences in the time scales of the dynamics of the plasma and the neutrals. These difficulties are overcome by the methods of time-slicing and subcycling.

The described code is employed to simulate the μAPPJ depicted in figure 1 with varying electrode gap sizes of 1.8, 1.0 and 0.3 mm. We choose these values to characterize the three regimes of plasma bulk-sheath ratios. The simulation resolves

the two Cartesian dimensions x and z. In the y direction, translational invariance is assumed.

Through leaks in the gas supply system as well as intrusion of air from the exit nozzle of the jet, the amount of nitrogen and oxygen in the feed gas is significant and has to be taken into account for the modelling approach. We mimic the impurities of the experimental setting according to [21] by adding 0.016% of nitrogen and 0.004% oxygen in the chemical model (Nitrogen and oxygen species have an impact on the quenching of the helium metastable density, oxygen additionally contributes to the electronegativity of the plasma). We consider the following species: Ground-state neutrals N_2, O_2, O, O_3 and He, $O_2(\nu)$, representing the first four vibrational levels of O_2, the electronically excited states N_2^* (a composite species representing all electronically excited N_2), $O_2(^1\Delta_g)$, $O_2(^1\Sigma_g^+)$, $O(^1D)$, $O(^1S)$, and $He^* \equiv He(^3S_1)$, $He_2^* \equiv He_2(^3\Sigma_u^+)$, positive ions N_2^+, O_2^+, O^+, He^+ and He_2^+, negative ions O_2^-, O^- and O_3^-, and electrons. The collisional cross sections of electron induced collisions and rate coefficients for the interactions of heavy particles are based on [22, 23] with extensions following [24, 25], and references therein. The flow rate of the gas mixture injected in the jet is adjusted to achieve advective gas velocities of about 100 m s^{-1}. The outlet is controlled to maintain a constant pressure. Finally, the secondary electron emission coefficient of the electrode surfaces depends on the ion and metastable species and varies from 0.26 for He^+, 0.22 for He_2^+, 0.11 for N_2^+, 0.12 for O^+, to 0.06 for O_2^+. We take the same values for the corresponding metastable species. Secondary electron emission due to electron bombardment and photons is neglected.

3. Results and discussion

3.1. Spatial distribution of He metastable atoms

Figure 3 shows 2D-maps of the He ($^3S_1$) metastable density in the discharge volume. The upper map shows experimental results whereas the bottom map shows simulation data. The horizontal and vertical axis span the exact area between the electrodes. The map of the experimental data, which covers 2000 reading points (40 vertical x 50 horizontal) of the absorption signal, in the plasma volume is in good qualitative and quantitative agreement with the simulation results. It should be mentioned that the steps occurring in the measured map at certain positions are due to mechanical limitations in the set-up, that made it necessary to record that map in four successive intervals. Furthermore, the measurement time for the map was several days, explaining why the map shows heavy fluctuations, whereas the actual metastable distribution in the discharge is more smooth, as seen in the measurements presented later in this paper.

A variety of effects determines the metastable distribution in the horizontal and the vertical axis. In horizontal direction the density profile is governed mainly by two effects. One is the alignment of the electrodes, since the electric field distribution strongly influences the electron energy. In the present experimental case the electrode gap is marginally
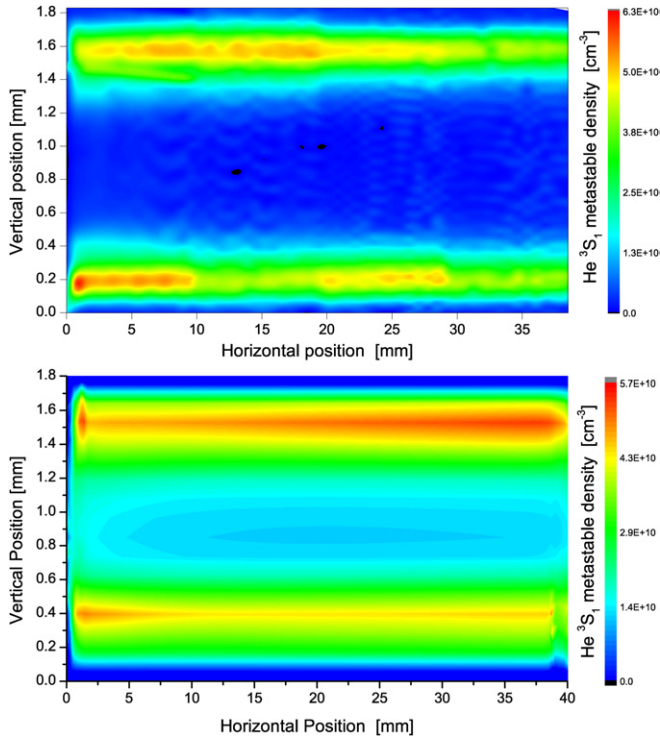
J. Phys. D: Appl. Phys. **44** (2011) 485204

B Niermann *et al*

Figure 3. Top: two-dimensional map of the measured metastable density in the discharge volume for the He $2^3S_1 \rightarrow 2^3P^0_{1,2}$ transition. Powered electrode at the top, grounded electrode at the bottom. Electrode gap width was 1.8 mm. Densities are given in cm^{-3}. Bottom: Simulation results for the spatial distribution of the He metastables.

Figure 4. Measured vertical metastable profile for gap widths between 2.7 mm and 0.25 mm.

larger on the rear side of the jet, resulting in a slight decrease in densities from left to right. A second and most important impact is given by impurities entering the jet through the exit nozzle, therewith quenching the metastable atoms. Since the jet is running permanently in contact with the ambient atmosphere the intrusion of nitrogen and oxygen into the plasma channel is significant, and decreases the metastable density especially in the first millimetres from the nozzle. Operating the jet in a clean helium atmosphere results in a homogenous density profile along the whole plasma column between the electrodes. The small fluctuations in the horizontal profile (which are not resolved by the simulation model) can be attributed to turbulences, imperfections in the surface of the electrodes or singularities in the walls of the gas channel.

The vertical metastable profile is less determined by these environmental factors but by the electron density and temperature distribution. The observed structure is consistent with the sheath structure in an RF discharge. Directly in front of the electrodes, the metastable density is low since the electron density is too low for an efficient excitation and ionization of the ground-state atoms (see also figure 4). Metastables reach their highest densities some $100\,\mu$m away from the electrode at the plasma–sheath interface, where in the negative glow area most excitation and ionization processes occur. Here in the sheath/bulk interface the electron energy is highest. In the bulk, the electric field strength
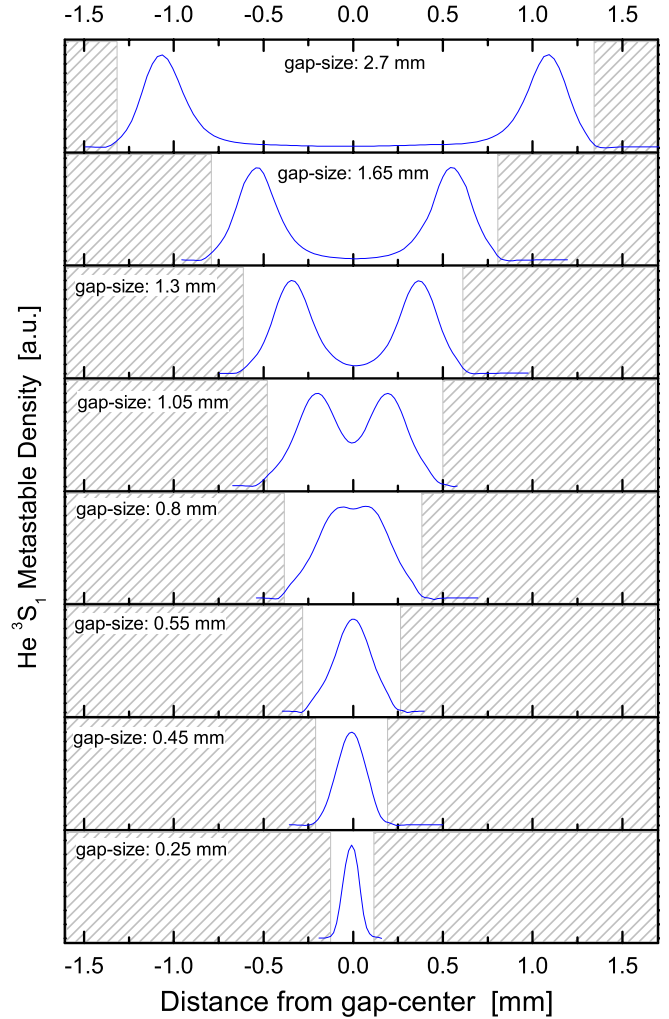
and therewith the electron temperature is low (see also figure 5), yielding to a lower metastable production rate. The asymmetry in the vertical profile of the simulated data can be attributed to stochastic effects in the simulation since it is not averaged over many RF-cycles due to runtime considerations, while the measurements are averaged over several 10^6 cycles.

3.2. Gap width variations

Due to the variability of the electrode gap the micro-plasma jet offers the possibility to continuously tune the sheath/bulk ratio and therewith the vertical excitation profile. Figure 4 shows the He metastable profile for gap widths between 2.7 and 0.25 mm. These values represent the limits where the pure helium discharge can be operated in α-mode. With decreasing gap width the breakdown voltage decreases while approaching the Paschen minimum. Figure 4 gives no quantitative values for metastable densities, since the gap width correlates with a variety of discharge parameters, like the impedance, the power coupling or the gas velocity, that all influence the species' density. Thus, a direct density comparison between different gap sizes is not expedient. Nevertheless it should be mentioned

that for a small gap width of 0.25 mm it was possible to produce much higher metastable densities than was possible for large gap sizes of 2.7 mm. For a gap width of about 1.5 cm the maximum metastable density achievable was in the order of 10^{11} cm^{-3} while for 0.25 cm gap widths values of 10^{13} cm^{-3} could be reached. The graphs show a steep rise of the density in front of the electrode surface with a maximum in the sheath/bulk interface, while in the bulk the density is low. The density distribution suggests that diffusion processes play a minor role for the metastable profile. At atmospheric pressure the mean free path of the electrons is short. High energetic electrons are lost in the sheath and can not contribute to the excitation in the plasma bulk. Although the metastable lifetime is comparatively long, in the order of $1\,\mu$s, the metastable diffusion to the bulk can be neglected likewise [21].

De-excitation of these species is dominated by three-body collision with ground-state atoms as well as quenching reaction with impurities, such as molecular nitrogen and oxygen. A detailed analysis of metastable lifetimes in this discharge is given in [21]. Three different regimes can be distinguished in the excitation profiles: Small sheath/bulk ratio (electrode gap > 2 mm), large sheath/bulk ratio (electrode gap around 1 mm), and a discharge without visible plasma bulk (electrode gap around < 0.5 mm). For gap widths larger than 1 mm the two excitation areas are clearly separated by the plasma bulk. Lowering the electrodes distance leads to the coalescence of the two sheath regions, and an excitation profile where highest densities are in the centre of the gap. For electrode distance of just a few hundred μm the plasma transforms to a pure 'sheath discharge'. These experimental findings are supported by the results from the numerical simulation. Figure 5 (top) shows the metastable profile for selected gap widths, the related electron densities and electron temperatures are given in figure 5 (bottom). The small admixture of oxygen into the feed gas in the simulation leads to an electronegativity of the plasma of about 0.1. Due to the lower ionization thresholds compared with helium species the positive ions are dominated by O$_2^+$ and N$_2^+$. The electron temperature profile for a gap width of 1.8 mm represents the excitation pattern of the metastable atoms. The temperatures are highest in the sheath/bulk interface, with a maximum of about 3 eV. Lowering the gap widths results, like in the experiment, in a convergence of the two sheaths. For a low gap width of 0.3 mm the electron density increases significantly, while temperatures reach values of almost 4 eV. This behaviour suggests that the high energy tail of the EEDF is getting more pronounced. Since the high electron energies enhance the production of metastable atoms, the simulation again supports the qualitative observation of very high metastable densities for low gap widths.

For metastable density measurements no error bars are shown, since statistical as well as systematic errors are negligible. For the presented data they are in the order of 10^9 cm^{-3}, while the density values are in the order of 10^{11}–10^{13} cm^{-3}. Due to the use of lock-in technique a sensitive measurement of low densities was possible with a high signal-to-noise ratio. A minor systematic error is caused by the unknown metastable profile in the *y*-axis, and the
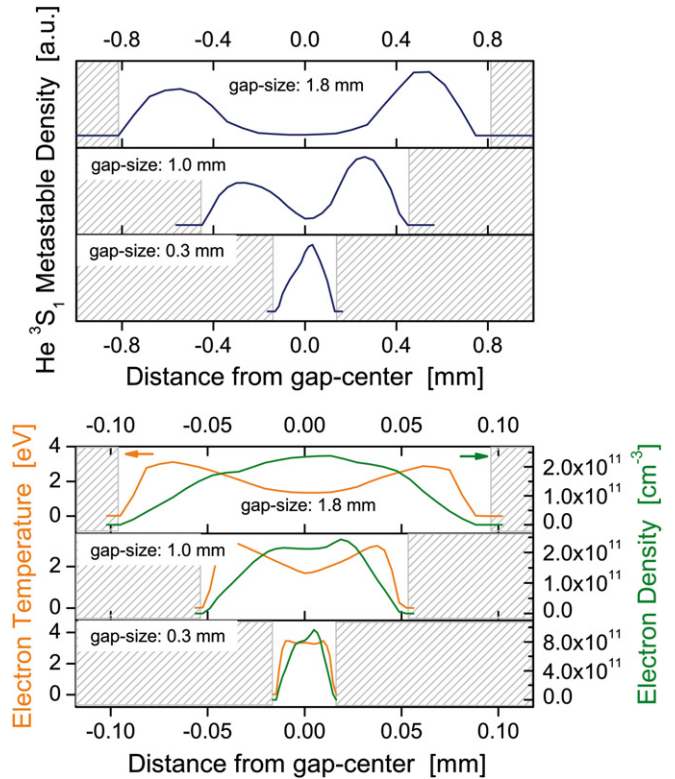

Figure 5. Top: Simulation results of characteristic metastable profiles for various gap widths. Bottom: Simulation results of electron density and electron temperature profiles for various gap widths.

implications on the absorption length. But since the metastable production and loss processes take place on a very local scale at atmospheric pressure, the profile in the *y*-axis is expected to be homogeneous with the exception of a tiny volume in front of the glass windows that confines the plasma channel and acts as a sink for metastable atoms.

4. Summary

We have shown that the experimental results for metastable distributions in micro-plasma jet discharges can be reproduced qualitatively and quantitatively by a 2D numerical model, therewith revealing the underlying excitation mechanisms of the discharge. By varying the gap width it was proven that the simulation model reliably mimics the experimental results for a large span of sheath bulk ratios. This now offers new possibilities in the analysis of extreme discharge conditions, like γ-mode structures and very small gap widths, showing effects like no quasi-neutrality all over the discharge volume.

Acknowledgments

References

[1] Katsch H M, Quand E and Schneider T 1996 *Plasma Phys. Control. Fusion* **38** 183
[2] Flohr R, Melzer A and Piel A 1994 *Plasma Sources Sci. Technol.* **3** 206
[3] Miclea M, Kunze K, Heitmann U, Florek S, Franzke J and Niemax K 2005 *J. Phys. D: Appl. Phys.* **38** 1709
[4] Tachibana K, Kishimoto Y and Sakai O 2005 *J. Appl. Phys.* **97** 123301
[5] Niermann B, Böke M, Sadeghi N and Winter J 2010 *Eur. Phys. J.* D **60** 489
[6] Schulz-von der Gathen V, Buck V, Gans T, Knake N, Niemi K, Reuter S, Schaper L and Winter J 2007 *Contrib. Plasma Phys.* **47** 510
[7] Schaper L, Reuter S, Waskoenig J, Niemi K, Schulz-von der Gathen V and Gans T 2009 *J. Phys. Conf.* **162** 012013
[8] Waskoenig J, Niemi K, Knake N, Graham L M, Reuter S, Schulz-von der Gathen V and Gans T 2010 *Plasma Sources Sci. Technol.* **19** 045018
[9] Kushner M J 2004 *J. Appl. Phys.* **95** 846
[10] Schütze A, Jeong J Y, Babayan S E, Park J, Selwyn G S and Hicks R F 1998 *IEEE Trans. Plasma Sci.* **26** 1685
[11] Knake N, Reuter S, Niemi K, Schulz-von der Gathen V and Winter Jörg 2008 *J. Phys. D: Appl. Phys.* **41** 194006
[12] Raizer Y P, Shneider M N and Yatsenko N A 1995 *Radio-frequency Capacitive Discharges* (Boca Raton, FL: CRC Press)
[13] Shi J and Kong M G 2006 *Phys. Rev. Lett.* **96** 105009
[14] Liu D W, Iza F and Kong M G 2009 *Appl. Phys. Lett.* **95** 031501
[15] Liu D W, Iza F and Kong M G 2008 *Appl. Phys. Lett.* **93** 261503
[16] Sadeghi N 2004 *J. Plasma Fusion Res.* **80** 767
[17] Babaeva N Y, Arakoni R and Kushner M J 2007 *J. Appl. Phys.* **101** 123306
[18] Babaeva N Y and Kushner M J 2007 *J. Appl. Phys.* **101** 113307
[19] Babaeva N Y and Kushner M J 2009 *Plasma Sources Sci. Technol.* **18** 035009
[20] Hemke T, Wollny A, Gebhardt M, Brinkmann R P and Mussenbrock T 2011 *J. Phys. D: Appl. Phys.* **44** 285206
[21] Niermann B, Kanitz A, Böke M and Winter J 2011 *J. Phys. D: Appl. Phys.* **44** 325201
[22] Stafford D S and Kushner M J 2004 *J. Appl. Phys.* **96** 2451
[23] Sommerer T J and Kushner M J 1992 *J. Appl. Phys.* **71** 1654
[24] Liu D-X, Rong M-Z, Wang X-H, Iza, F, Kong M G and Bruggeman P 2010 *Plasma Process. Polym.* **7** 846
[25] Sakiyama Y and Graves D B 2007 *J. Appl. Phys.* **101** 073306